

# **The chemistry of Cu<sub>3</sub>N and Cu<sub>3</sub>PdN nanocrystals**

Mahsa Parvizian<sup>1</sup>, Alejandra Duràn Balsa<sup>1</sup>, Rohan Pokratath<sup>1</sup>, Curran Kalha<sup>2</sup>, Seungho Lee<sup>3</sup>,  
Maria Ibáñez<sup>3</sup>, Anna Regoutz<sup>2</sup>, Jonathan De Roo<sup>1\*</sup>

<sup>1</sup> Department of Chemistry, University of Basel, Basel CH-4058, Switzerland

<sup>2</sup> Department of Chemistry, University College London, 20 Gordon Street, London, WC1H  
0AJ, United Kingdom.

<sup>3</sup> IST Austria, Am Campus 1, 3400 Klosterneuburg, Austria

\* Corresponding author: Jonathan De Roo, [Jonathan.DeRoo@unibas.ch](mailto:Jonathan.DeRoo@unibas.ch)

## Abstract

Cu<sub>3</sub>N and Cu<sub>3</sub>PdN nanocrystals are attractive materials with numerous applications ranging from optoelectronics to catalysis. However, their chemical formation mechanism and surface chemistry are unknown or contested. In this work, we first optimize the synthesis and purification to yield phase pure, colloidal stable Cu<sub>3</sub>N and Cu<sub>3</sub>PdN nanocubes. Second, we elucidate the precursor conversion mechanism that leads to the formation of Cu<sub>3</sub>N from copper(II) nitrate and oleylamine. We find that oleylamine is both the reductant and nitrogen source. Oleylamine is oxidized to a primary aldimine and the latter reacts further with oleylamine to a secondary aldimine, eliminating ammonia. Ammonia reacts with Cu(I) to form Cu<sub>3</sub>N. Third, we investigated the surface chemistry of the nanocrystals using solution NMR spectroscopy and X-ray photoelectron spectroscopy (XPS). We find a mixed ligand shell of aliphatic amines and carboxylates. The carboxylate is produced *in situ* during the synthesis. While the carboxylates appear tightly bound, the amines are easily desorbed from the surface. Finally, we analyze the optoelectronic properties by UV-Vis and XPS. Doping with palladium decreases the bandgap but the material remains a semiconductor. These results bring insight into the chemistry of metal nitrides and will help the development of other metal nitride nanocrystals.

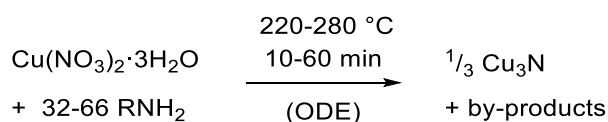
## Keywords

Nitride, copper nitride, structural analysis, mechanism, surface chemistry, ligands

## Introduction

Metal nitrides are a versatile class of materials with increasing interest.<sup>1-3</sup> Copper nitride ( $\text{Cu}_3\text{N}$ ) specifically has garnered attention as an inexpensive, non-toxic material with potential applications in solar cells,<sup>4</sup> high-density optical data storage,<sup>5</sup> and electrocatalysis (oxygen evolution and  $\text{CO}_2$  reduction).<sup>6-8</sup>  $\text{Cu}_3\text{N}$  is a semiconductor with a calculated indirect bandgap of 1 eV and an anti- $\text{ReO}_3$  cubic crystal structure.<sup>4, 9, 10</sup> The body center position can be occupied by dopants (e.g., palladium) forming structures such as  $\text{Cu}_3\text{Pd}_x\text{N}$ . Upon doping, the lattice constant increases,<sup>11, 12</sup> and the electronic structure of the material is reported to change from semiconducting to (semi)-metallic.<sup>13, 14</sup>

Bulk  $\text{Cu}_3\text{N}$  forms at relatively low temperature but decomposes at higher temperature ( $475^\circ\text{C}$ ) to metallic copper (under inert atmosphere) or copper oxide (in air).<sup>5, 15</sup> The first wet-chemical synthesis of bulk  $\text{Cu}_3\text{N}$  powders were based on aminolysis or the solvothermal decomposition of copper azides.<sup>15-17</sup> Ultra-small (2-4 nm) and colloidally stable nanocrystals of  $\text{Cu}_3\text{N}$  have been synthesized from  $\text{Cu}(\text{OMe})_2$  in benzylamine,<sup>18</sup> or by aminolysis of  $\text{Cu}(\text{I})$  in pyridine.<sup>19</sup> Larger colloidal  $\text{Cu}_3\text{N}$  nanocubes have been obtained from copper nitrate and alkylamine, see Scheme 1.<sup>6, 8, 20-23</sup> In most cases, additional solvent is added (usually 1-octadecene, ODE). The equivalents of ligand (32-66), the reaction temperature ( $220\text{-}280^\circ\text{C}$ ), and time (10-60 min) vary, as does the nature of the alkyl chain of the amine (oleylamine, hexadecylamine or octadecylamine). Changing the nature of the amine allows to tune the final size from 10 to 25 nm.



**Scheme 1.** The range of conditions reported for the synthesis of colloidal  $\text{Cu}_3\text{N}$  nanocrystals.

Unfortunately, the reaction mechanism and the by-products are not well established. Some authors claim that nitrate is the nitrogen source, and thus nitrogen is supposed to be reduced

from its highest oxidation state in nitrate to its lowest oxidation state in nitride, and this process is presumably catalyzed by the amine ligand.<sup>22</sup> Other authors assume that Cu(II) is first fully reduced to Cu(0) and subsequently reacts with dinitrogen (a possible decomposition product of the nitrate complex).<sup>24</sup> However, there is currently insufficient evidence to claim a mechanism for the precursor conversion. Regarding the crystallization mechanism, it was shown that first small, amorphous particles form, which subsequently ripen into Cu<sub>3</sub>N nanocubes.<sup>8</sup>

The surface chemistry of Cu<sub>3</sub>N nanocrystals is also unknown. Although alkylamines are the only ligand present during the synthesis, there are several examples where the ligands can convert to other ligands during nanocrystals synthesis, leading to surprising surface chemistries.<sup>25, 26</sup> Given the importance of surface chemistry for nanocrystal applications it is imperative to elucidate and control it.<sup>27</sup> Amines typically bind to the nanocrystal surface as Lewis basic (L-type) ligands and feature an adsorption-desorption equilibrium that is often highly dynamic.<sup>28-30</sup> However, in the case of copper based nanocrystals, amines have been observed to be tightly bound.<sup>31, 32</sup> It is thus surprising that Cu<sub>3</sub>N nanocrystals have generally poor colloidal stability after purification.

In this work, we aimed at elucidating the precursor conversion mechanism and surface chemistry of Cu<sub>3</sub>N (and Cu<sub>3</sub>PdN) nanocrystals, synthesized from copper nitrate (and palladium acetylacetonate). We first screened the different synthetic methods in the literature, and found the report of Vaughn *et al.* as the most reproducible.<sup>21, 33</sup> We then explored the influence of different parameters on the reaction outcome, including the presence of water, temperature, time, etc. Having obtained the optimal conditions to form phase pure Cu<sub>3</sub>N nanocubes, we then redesigned the purification procedure to yield colloidally stable Cu<sub>3</sub>N nanocrystals. We uncovered the precursor conversion mechanism of the reaction. We found that nitrate and Cu(II) both oxidize alkylamine to a primary aldimine, forming also Cu(I). Condensation of the primary aldimine with a second equivalent alkylamine, yields a secondary aldimine and ammonia. The

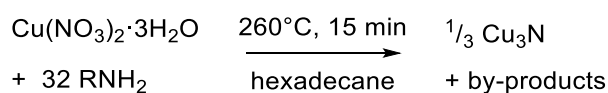
latter is the active nitrogen precursor and reacts with Cu(I) to Cu<sub>3</sub>N. Finally, the surface of these Cu<sub>3</sub>N and Cu<sub>3</sub>PdN particles have been analyzed. X-ray photoelectron spectroscopy (XPS) and FTIR established the presence of carboxylate ligands on the surface, together with amine ligands. Advanced nuclear magnetic resonance (NMR) spectroscopy revealed the dynamics of ligands binding. These fundamental chemistry insights will enable the elucidation of formation mechanisms of other copper-based colloidal nanocrystals and other metal nitrides.

## Results and discussion

**Synthesis optimization.** We decided to optimize the procedure reported by Vaughn *et al.* by exploring the influence of different parameters.<sup>21</sup> First, we replaced 1-octadecene (the solvent) with hexadecane since we reported earlier that 1-octadecene polymerizes at 240 °C, contaminating the final nanocrystal product and complicating the purification.<sup>34</sup> Concerning reaction temperature, crystalline Cu<sub>3</sub>N was formed between 220 °C and 260 °C (for 15 minutes), with the highest crystallinity for 260 °C (Figure S1). Interestingly, the crystallite size was found to be quite independent of the reaction temperature (10-11 nm according to the Scherrer analysis of the powder XRD (X-ray diffraction) reflections). At 200 °C, no particles could be isolated. Furthermore, we took reaction aliquots at 5, 10, 15, 30, and 60 min at 240 °C and 260 °C. Each aliquot was purified and analyzed by transmission electron microscopy (TEM) to observe the nanocrystal growth throughout the reaction. At 240 °C, we observed both small dots and fully formed nanocubes up to 15 min of reaction time (Figures S2). The small particles presumably ripen in the bigger nanocubes since the former disappear at 30 min. After 60 minutes at 240°C, the XRD showed pure Cu<sub>3</sub>N. By comparison, at 260 °C, the nanocubes were already fully formed after 15 min. After 30 min at 260°C, the particles started to decompose and crystalline Cu(0) was formed (Figure S3).

The reported procedure has two steps where vacuum is applied. This leads us to investigate the role of water and whether an inert atmosphere is strictly necessary. Note that the precursor

contains water (an equivalent of 13  $\mu\text{L}$  for a standard synthesis). We obtained identical  $\text{Cu}_3\text{N}$  nanocrystals when the vacuum steps were omitted, or, when after applying vacuum (presumably removing water), again 13  $\mu\text{L}$  of water was injected into the reaction mixture (Figures S4-S5). However, the same reaction in an open flask did not yield  $\text{Cu}_3\text{N}$  (or any isolatable material), indicating that an important gaseous intermediate can escape from the reaction mixture. To work under controlled and reproducible conditions, we still choose to perform a short (30 min) degassing step at 50  $^{\circ}\text{C}$ , but it appears that the synthesis is robust against air or water contamination. We also found that both 30 and 60 equivalents of amine ligands yielded  $\text{Cu}_3\text{N}$  nanocrystals (Figure S6). Based on the above optimization, we arrived at the conditions in Scheme 2.



**Scheme 2.** The conditions that lead most reproducibly to phase-pure  $\text{Cu}_3\text{N}$  nanocrystals.

**Colloidal stability.** After applying the reported precipitation-and-redispersion cycles (with ethanol and toluene),<sup>21</sup> the particles were redispersed in toluene (5 mL), but they precipitated within a couple of minutes, see Figure 1. Since the nanocrystals were colloidally stable in the crude reaction mixture, we hypothesized that the ligands desorbed from the surface during the precipitation-and-redispersion cycles. The nature and volume of the solvent used for redispersion play an important role since they determine the position of the adsorption-desorption equilibrium. The ligand-solvent interaction should be favorable enough to disperse the nanocrystals, but not so high that ligands prefer to be fully solvated over being bound to the surface.<sup>35</sup> During purification, it is also preferred to work with quite concentrated dispersions to minimize the loss of nanocrystals over several cycles. On the other hand, too high concentrations might cause impurities to be trapped between the flocculating nanocrystals. Considering the above points, we adapted the purification procedure. Various solvents (toluene,

hexane, chloroform, and cyclohexane), as well as non-solvents (acetone, ethanol, and methanol), were tested. Our final procedure involves two precipitation cycles with acetone (15 mL) followed by a final precipitation with ethanol (15 mL), always redispersing in cyclohexane (5 mL).<sup>36</sup> A 10 v% solution of distilled oleylamine was added after the first acetone wash (1 mL) and after the second acetone wash (2 mL) followed by 5 minutes of sonication. There was no need for a final oleylamine addition after the ethanol wash and the nanocrystals remained colloidally stable. This procedure thus minimized the amount of excess ligand in the final product but provided a stable dispersion (11 mg/mL) of oleylamine capped Cu<sub>3</sub>N nanocrystals, see Figure 1. From thermogravimetric analysis (TGA), we determined that the dried samples contained 29.2 w% organics (ligands) and the final Cu<sub>3</sub>N yield is 96 %.



**Figure 1.** Photograph of Cu<sub>3</sub>N nanocrystals after regular (left) and optimized (right) purification.

Copper palladium nitride (Cu<sub>3</sub>PdN) nanocrystals were also synthesized. The procedure was identical to that of Cu<sub>3</sub>N, except for the reaction temperature (240°C) and the addition of 0.33 equivalents of Palladium(II) 2,4- pentadionate alongside the Cu(NO<sub>3</sub>)<sub>2</sub>. The doped nanocrystals were purified with the optimized purification method. The synthesis yielded black nanoparticles that were colloidally stable (13 mg/ mL). According to TGA, ligands make up 13.22 w% of the dried mass (assuming perfect Cu<sub>3</sub>PdN stoichiometry) and the Cu<sub>3</sub>PdN yield is 91 %.

**Structural analysis.** The final dispersions of Cu<sub>3</sub>N and Cu<sub>3</sub>PdN nanocrystals were analyzed with TEM, XRD and dynamic light scattering (DLS) (Figure 2). According to TEM, the average

cube edge length is 13.5 nm ( $\sigma = 1.9$  nm) for the Cu<sub>3</sub>N nanocubes and 10.2 nm ( $\sigma = 1.4$  nm) for the Cu<sub>3</sub>PdN nanocrystals. The solvodynamic diameter obtained from DLS analysis were 17 nm for Cu<sub>3</sub>N and 13 nm for Cu<sub>3</sub>PdN. The sizes obtained via DLS are in line with the sizes obtained via TEM since DLS determines the solvodynamic size of the whole particle, including the surface ligands. Both TEM and DLS support that the dispersions are highly stable since no aggregates are observed. XRD shows quite sharp reflections for Cu<sub>3</sub>N (crystallite size =  $9.0 \pm 1.7$  nm), while they are broader for Cu<sub>3</sub>PdN (crystallite size =  $4.5 \pm 1.1$  nm). Compared with the sizes obtained from TEM, it is clear that the Cu<sub>3</sub>PdN nanocrystals are polycrystalline. A real space refinement of the Pair Distribution Function further confirms the structure of Cu<sub>3</sub>N and Cu<sub>3</sub>PdN (Figure S7).

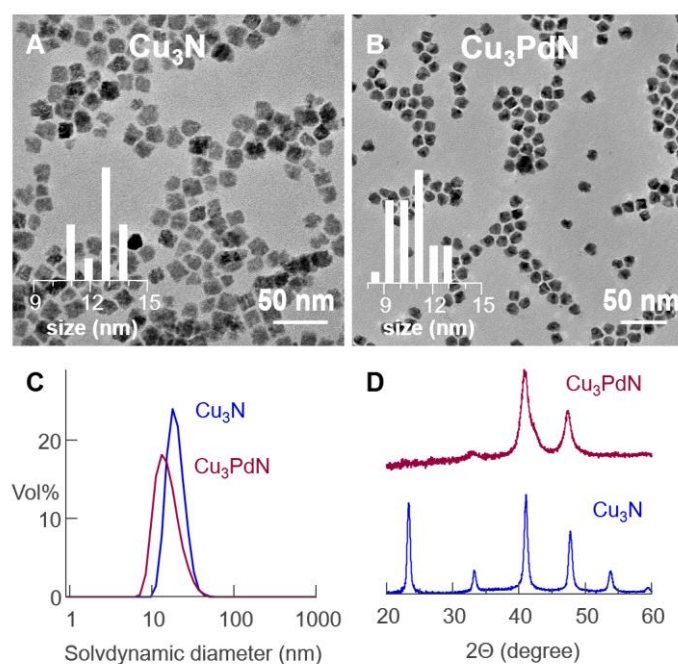
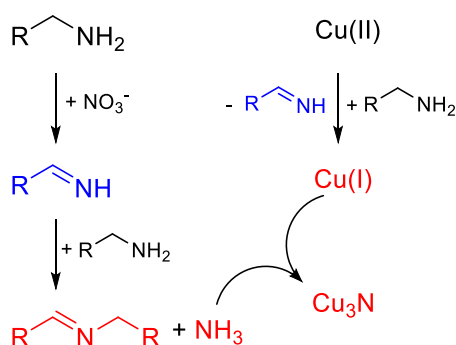


**Figure 2.** TEM images of (A) Cu<sub>3</sub>N and (B) Cu<sub>3</sub>PdN. The histograms are shown as an inset. The cube edge length is used as a measure for size. (C) DLS and (D) powder XRD measurements.

**Precursor conversion mechanism.** We found the proposed pathways in literature implausible and therefore proposed an alternative hypothesis in which the active nitride source is ammonia,



see Scheme 3. First, oleylamine is oxidized to a primary aldimine by nitrate. Nucleophilic addition of a second equivalent of oleylamine forms the more stable, secondary aldimine with the elimination of ammonia. Ammonia reacts with Cu(I) to Cu<sub>3</sub>N. The Cu(I) species was generated by reduction of Cu(II) by oleylamine upon heating. Cyclic voltammetry confirms a lower reduction potential of Cu(II) to Cu(I) upon addition of oleylamine (at room temperature).<sup>37</sup> We hypothesize that the co-product of this Cu(II) reduction is the same primary aldimine as mentioned before.



**Scheme 3.** Our proposed pathway for Cu<sub>3</sub>N formation. Precursors are shown in black, detected species in red, and hypothesized intermediates in blue.

The copper precursor, Cu(NO<sub>3</sub>)<sub>2</sub>·3H<sub>2</sub>O, does not dissolve in the solvent (hexadecane) until oleylamine is added, indicating the formation of a coordination complex. This is supported by the deep blue color of the reaction mixture, typical for Cu(II) coordinated by amines.<sup>38, 39</sup> During the heat-up to 260 °C, the color of the solution changes from blue to yellow around 185°C, indicating the reduction of Cu(II) to Cu(I). Concomitant with the color change, new resonances appear in the <sup>1</sup>H NMR spectrum of the reaction mixture, see Figure 3. We assign these resonances to the secondary aldimine. Upon reaching the reaction temperature (240-260°C), the reaction mixture turns black (indicating the formation of Cu<sub>3</sub>N), and we observe in the <sup>1</sup>H NMR spectrum a significant increase in the aldimine concentration (Figure 3). We confirmed the identity of the aldimine by synthesizing the secondary aldimine of dodecyl aldehyde and octadeylamine, and we found perfect agreement of the resonances **1-3**.

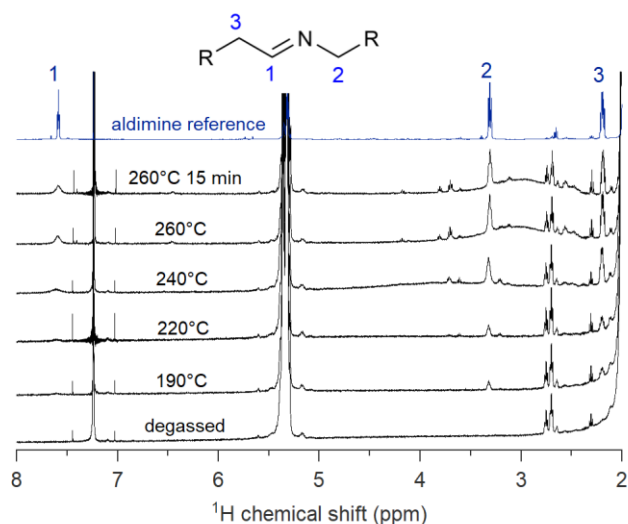
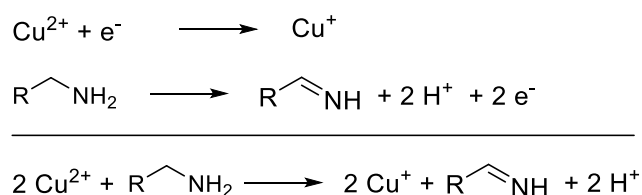


Figure 3.  $^1\text{H}$  NMR spectra of aliquots after degassing, at  $190^\circ\text{C}$  after the color change,  $220^\circ\text{C}$ ,  $240^\circ\text{C}$ ,  $260^\circ\text{C}$  and at the end of the reaction. Aldimine formation is observed starting from the color change. The aldimine reference is shown for comparison.

Ammonia is detected in the reaction mixture by bubbling Ar through the reaction mixture during synthesis, and dissolving the gasses in either 40 mL or 80 mL water. A commercial ammonia test kit indicates a concentration of 200 mg/L or 100 mg/L respectively (Figure S8). Given that the reaction is executed at a scale of 0.24 mmol Cu, and assuming that every nitrate (0.48 mmol) oxidizes one oleylamine molecule, this is the expected amount of ammonia (0.48 mmol, 8 mg). We can also quantify the aldimine formation by using the alkene resonance of oleylamine as the internal standard. For every aldimine, we find 18 oleyl chains, indicating a conversion of 5.5 %. Given that 7.6 mmol oleylamine was used, this amounts to 0.42 mmol aldimine. This value is in reasonable agreement with the amount of ammonia detected (taking into account the error on the ammonia measurement and the fact that oleylamine is only 70 % pure). This quantitative picture thus confirms our hypothesis and indicates a one-to-one stoichiometry between nitrate, aldimine, and ammonia. We did not obtain  $\text{Cu}_3\text{N}$  in this experiment since we removed ammonia from the reaction mixture. This indicates that ammonia is essential in nitride formation.

We also quantified the small amount of aldimine (0.1 mmol) generated during the reduction of Cu(II) to Cu(I). This value is about half of the copper amount (0.24 mmol) and can be easily rationalized based on electron counting in the redox reactions. Indeed, the reduction of Cu(II) to Cu(I) is a one-electron process while the oxidation of primary amine to aldimine is a two-electron process, see Scheme 4. The scheme also makes clear that the oxidation of primary amine generates a large amount of protons which are presumably absorbed by the excess oleylamine. These protons are observed in the  $^1\text{H}$  NMR spectrum as a broad resonance around 3 ppm (see Figure 3). They do not appear in the typical region for alkylammonium resonances, since maximally 1.2 mmol protons are generated and oleylamine is still present in excess (7 mmol). Given that proton equilibria are typically fast, we thus observe the population averaged chemical shift between protonated oleylamine and unprotonated oleylamine.



**Scheme 4.** Redox half reactions and overall reaction for the reduction of  $\text{Cu}^{2+}$  by primary amines.

Our proposed pathway requires a primary amine. To further test our hypothesis, we thus attempted the synthesis of  $\text{Cu}_3\text{N}$  with dioctylamine and trioctylamine. As expected, the reaction did not produce  $\text{Cu}_3\text{N}$  but  $\text{Cu}_2\text{O}$  instead, see Figure 4. Also in the NMR spectrum, we do not find aldimine in the case of trioctylamine and only a very small amount in the case of dioctylamine. The latter can be directly oxidized to a secondary aldimine, without a primary aldimine intermediate (and thus without ammonia elimination) (Figure S9).

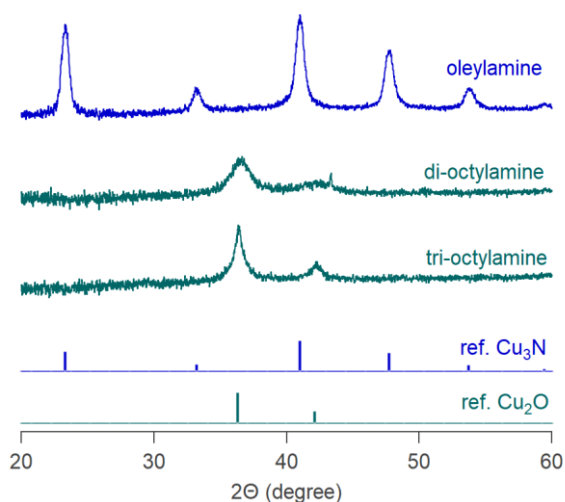


**Figure 4.** XRD spectra of the syntheses with different amines. The reference of bulk  $\text{Cu}_3\text{N}$  (blue) and bulk  $\text{Cu}_2\text{O}$  (green) are shown.

We thus firmly established that nitrate is not the nitrogen source for  $\text{Cu}_3\text{N}$  but rather oxidizes the amine to aldimine.  $\text{Cu}_3\text{PdN}$  nanocrystal follows the same mechanism based on the formation of aldimine and ammonia during the reaction (Figure S10). The mechanism is reminiscent of the one for  $\text{InN}$ , where  $\text{In}^{3+}$  oxidizes primary amines into aldimine and nucleophilic attack of lithium oleylamide generates amide,  $\text{NH}_2^-$ .<sup>40</sup> However, an important difference is that for copper, an additional oxidant (nitrate) is required. The reduction of  $\text{Cu}^{2+}$  alone does not seem to generate sufficient ammonia to form copper nitride since other copper salts do not generate copper nitride.<sup>22</sup> Or perhaps it generates ammonia at too low temperatures, where the formation of  $\text{Cu}_3\text{N}$  is not yet favored. More detailed insight into the crystallization mechanism of  $\text{Cu}_3\text{N}$  could shed light on this issue.

**Surface chemistry.** X-ray photoelectron spectroscopy (XPS) was used to explore the surface chemistry. Survey spectra for both compounds (Figure S11) show spectral signatures from all expected elements. In addition, a small amount of Si was detected most likely from the silicone grease used during the synthesis. The binding energy (BE) position of the main feature in the Cu  $2p_{3/2}$  core level ( $932.7 \pm 0.1$  eV) is commensurate with the expected Cu(I) oxidation state for

both samples (Figure 5(A)). In addition, both samples show a shoulder towards the higher BE of the main peak (marked with an asterisk in Figure 5(A)) and in the Cu<sub>3</sub>PdN sample, a clear Cu(II) satellite is also visible. From peak fit analysis (Figure S12), the contribution of these additional chemical states relative to the main Cu(I) line is  $12.3 \pm 0.5$  rel.at.% for Cu<sub>3</sub>N and  $17.9 \pm 0.5$  rel.at.% for Cu<sub>3</sub>PdN, respectively. The Pd 3*d* core level (Figure 5(B)) is only observed for the Cu<sub>3</sub>PdN sample. The BE of the Pd 3*d*<sub>5/2</sub> component ( $335.5 \pm 0.1$  eV) is commensurate with Pd(0) or Pd(I) with a spin-orbit-splitting of the doublet of 14.6 eV. In both samples, the N 1*s* core level (Figure 5(C)) displays two contributions. The lower BE feature at  $397.8 \pm 0.2$  eV corresponds to metal-nitride and the higher BE feature at  $399.6 \pm 0.2$  eV corresponds to the expected oleylamine ligand, bound to the nanocrystal surface. The O 1*s* core level (Figure 5(D)) shows three discernible contributions from metal oxide, metal hydroxide, and carboxylate environments. Together with the Cu(II) species, we infer that the surface of the particles contains an amorphous copper oxyhydroxide layer. The carboxylate is assigned to a surface bound oleate ligand and its presence is also detected by FTIR (broad signal at  $1577\text{ cm}^{-1}$ , see Figure S13). Oleate is most likely formed by oxidation of oleylamine by nitrate, as we reported earlier in the synthesis of cerium oxide nanocrystals.<sup>26</sup>

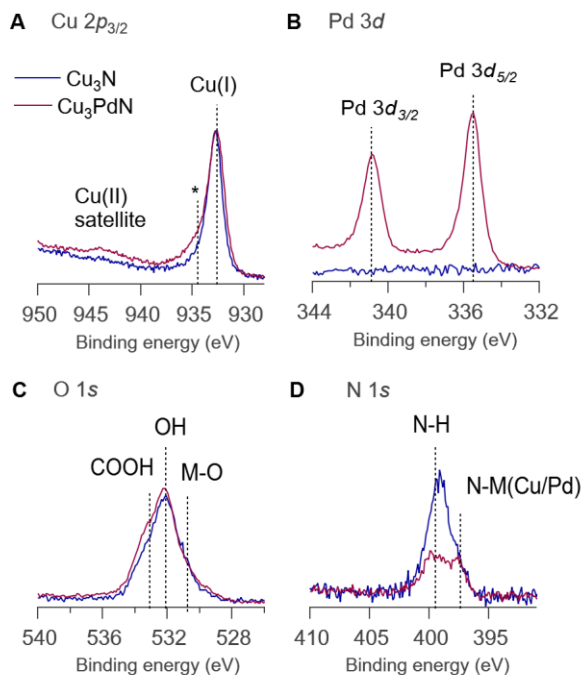


**Figure 5.** XPS core level spectra of Cu<sub>3</sub>N and Cu<sub>3</sub>PdN, including (A) Cu 2p<sub>3/2</sub>, (B) Pd 3d, (C) O 1s and (D) N 1s.

The <sup>1</sup>H NMR spectra of Cu<sub>3</sub>N and Cu<sub>3</sub>PdN show the typical signature of an oleyl chain (Figure 6). While the alkene resonance is reasonably sharp, the resonances close to the binding group are indistinguishable from the background. This broadening is likely due to fast T<sub>2</sub> relaxation induced by copper.<sup>32</sup> Based on the line width of the alkene resonance,<sup>41</sup> we inferred that the ligand is dynamic and in fast exchange between a bound and free state. This is confirmed by a relatively high diffusion coefficient ( $D = 174 \mu\text{m}^2/\text{s}$ ) determined by pulsed field gradient experiments on the Cu<sub>3</sub>N dispersion (Figure S14). For Cu<sub>3</sub>PdN, we noticed a second, very broad alkene resonance of low intensity underneath the sharp signal. A careful pulsed field gradient experiment revealed that the alkene resonance is a superposition of two species, one diffusing with  $D = 48 \mu\text{m}^2/\text{s}$  and the other one with  $D = 667 \mu\text{m}^2/\text{s}$  (Figure 6 (B)). The small diffusion coefficient corresponds to a solvodynamic diameter of 17 nm (via the Stokes-Einstein equation), which agrees quite well with a nanocrystal of 12 nm and a ligand shell of 2 nm thickness. We thus assign the broad resonance to tightly bound ligand, presumably the oleate.

The larger diffusion constant corresponds most likely to oleylamine. We could only detect the tightly bound oleate in the Cu<sub>3</sub>PdN sample, but oleate is also present on the surface of Cu<sub>3</sub>N according to our XPS results, albeit to a lesser extent. Unfortunately, all signals appear more broadened in the Cu<sub>3</sub>N sample and the tightly bound oleate could not be detected.

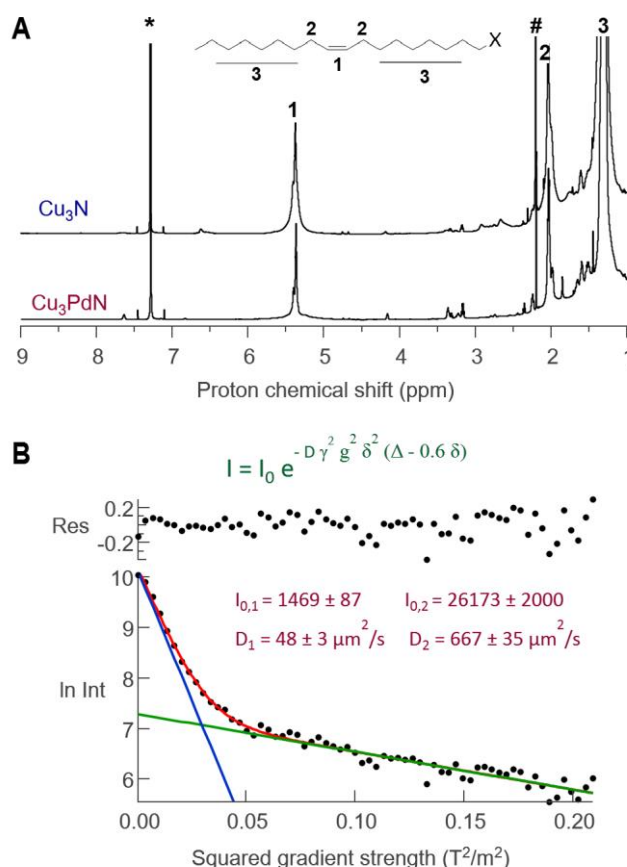


**Figure 6.** Nuclear magnetic resonance spectroscopy of the purified Cu<sub>3</sub>N and Cu<sub>3</sub>PdN NCs. (A) <sup>1</sup>H-NMR of the NCs indicating the presence of oleyl chain. (B) Diffusion ordered NMR spectroscopy of the Cu<sub>3</sub>PdN NCs showing a slow and a fast diffusing species.

**Optoelectronic characteristics.** In addition to the identification of the chemical states present in the samples, XPS was also used to probe the electronic structure of Cu<sub>3</sub>N and Cu<sub>3</sub>PdN by collecting valence band spectra. Figure 7(B) shows the valence band spectra of the two compounds, as well as the broadened and cross section weighted total density of states of Cu<sub>3</sub>N from density functional theory (DFT) calculations. The experimental and theoretical results for

Cu<sub>3</sub>N agree very well. The projected density of states calculations (Figure S15) show that the valence band of Cu<sub>3</sub>N is dominated by Cu 3*d* states with only minor mixing of Cu 3*p* states and minimal nitrogen contributions. The valence band maximum (VBM) position of Cu<sub>3</sub>N is  $0.55 \pm 0.05$  eV from the Fermi energy  $E_F$ . In comparison, the valence spectrum of Cu<sub>3</sub>PdN shows additional intensity towards the  $E_F$  from Pd states closing the VBM- $E_F$  gap. In parallel, UV-Vis has been used to determine the optical band gap of the particles. An indirect band gap has been reported for Cu<sub>3</sub>N thin films according to theoretical band structure calculations.<sup>4</sup> To our knowledge, the type of optical band gap (direct or indirect) has not yet been reported for Cu<sub>3</sub>PdN. In this work, we assumed an indirect optical bandgap for both samples. A Tauc plot analysis resulted in an optical bandgap of  $1.8 \pm 0.1$  eV and  $0.9 \pm 0.1$  eV for our Cu<sub>3</sub>N and Cu<sub>3</sub>PdN NCs, respectively (Figure 7 (A)). The reduction in optical band gap is commensurate with the closing of the electronic VBM- $E_F$  separation observed in XPS.

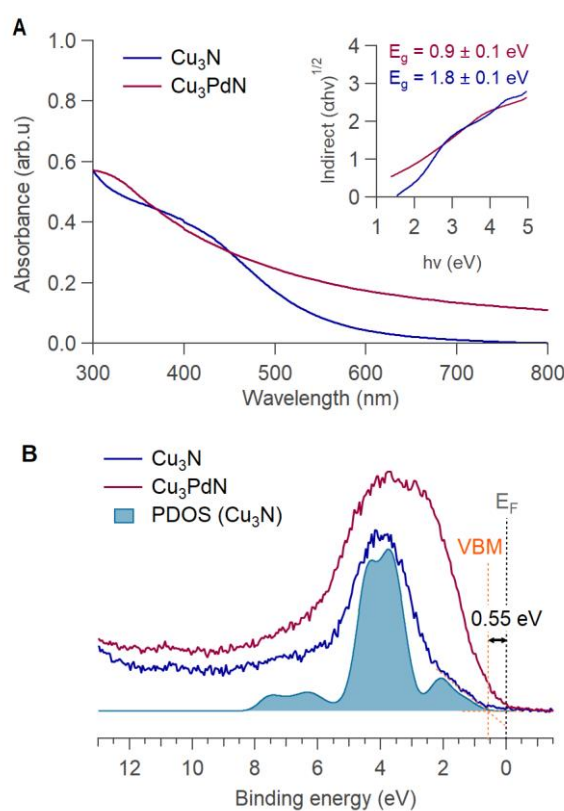


**Figure 7:** (A) UV-Vis absorption spectra of Cu<sub>3</sub>N and Cu<sub>3</sub>PdN and their corresponding Tauc plot as an inset. An indirect bandgap of  $1.8 \pm 0.1$  eV and  $0.9 \pm 0.1$  eV has been determined for Cu<sub>3</sub>N and Cu<sub>3</sub>PdN,



respectively. (B) Valence region of Cu<sub>3</sub>N and Cu<sub>3</sub>PdN, including XPS valence spectra and the broadened and cross section weighted sum of the projected density of states (PDOS) from density functional theory (DFT). The position of the valence band maximum (VBM) of Cu<sub>3</sub>N and the position of the Fermi energy (E<sub>F</sub>) are also shown.

## Conclusions

In conclusion, we successfully optimized the synthesis of Cu<sub>3</sub>N and Cu<sub>3</sub>PdN nanocrystals in order to obtain phase pure, colloiddally stable nanocrystals via modulating the reaction parameters with a focus on the purification. We provided experimental support for a precursor conversion pathway that hypothesized ammonia as the active nitrogen source. We proposed that primary aldimine is the oxidation product of the ligand (oleylamine), oxidized by both Cu(II), and nitrate. Nucleophilic addition and elimination of a second oleylamine molecule onto the primary aldimine released ammonia, which subsequently reacted with Cu(I) to form Cu<sub>3</sub>N and Cu<sub>3</sub>PdN. The surface of the nanocrystals was capped by a mixture of oleylamine and oleate. The latter was formed *in situ* from the further oxidation of aldimine. The addition of palladium to copper nitride reduces the optical band gap as well as the separation between the valence band maximum (VBM) and Fermi energy E<sub>F</sub>.

## Experimental section

**Materials.** For the standard copper nitride and copper palladium doped nitride nanoparticles, copper nitrate ( $\text{Cu}(\text{NO}_3)_2 \cdot 3\text{H}_2\text{O}$ , STREM Chemicals, 99.5 %) and distilled oleylamine ( $\text{C}_{18}\text{H}_{35}\text{NH}_2$ , Sigma-Aldrich, 70 %) were used as precursors in hexadecane ( $\text{C}_{16}\text{H}_{34}$ , Sigma Aldrich 99 %). Palladium(II) 2,4- pentadionate ( $\text{C}_{10}\text{H}_{14}\text{O}_4\text{Pd}$ , Alfa Aesar, Pd 34.7 %) was used for doping. For the mechanistic investigations, various precursors were used: copper chloride ( $\text{CuCl}_2 \cdot 2 \text{H}_2\text{O}$ , Sigma-Aldrich,  $\geq 99.0\%$ ), dioctylamine ( $\text{CH}_3(\text{CH}_2)_7\text{NH}-(\text{CH}_2)_7\text{CH}_3$ ), Sigma-Aldrich, 97 %), trioctylamine ( $(\text{CH}_3(\text{CH}_2)_7)_3\text{N}$ , Sigma-Aldrich, 98 %). For the aldimine synthesis, lauric aldehyde ( $\text{CH}_3(\text{CH}_2)_{10}\text{CHO}$ , Sigma-Aldrich,  $\geq 95\%$ ) was used. Cyclohexane, absolute ethanol and acetone were used for the purification step. Deuterated chloroform ( $\text{CDCl}_3$ , 98 %) was used for NMR study.

**Synthesis of  $\text{Cu}_3\text{N}$ .** The synthesis for  $\text{Cu}_3\text{N}$  nanocrystals was adapted from the literature. Copper nitrate (0.24 mmol, 60 mg, 1 eq) was dissolved in 7.5 mL of hexadecane in a three-neck flask and stirred. Distilled oleylamine (7.57 mmol, 2.5 mL, 31 eq) was added and the mixture was degassed for 30 minutes at 50 °C. Under argon, the temperature was increased to 260 °C at a rate of 10 °C per minute. The mixture was left to react for 15 minutes. The flask was then removed from the heating mantle and left to cool to room temperature over the course of an hour. The 10 mL solution of nanoparticles were transferred to centrifuge tubes. A total of 15 mL of acetone was added and the particles were centrifuged at 5 000 rpm for 3 minutes. The supernatant was removed and the particles were redispersed in 4 mL of cyclohexane. A 10% by volume stock solution (SS) of purified oleylamine in cyclohexane was prepared. Oleylamine (1 mL SS) was added to the redispersed particles, so the total redispersion volume was 5 mL. The particles were placed in the ultrasonic bath until fully redispersed. The particles were washed once more with acetone (15 mL) and this time redispersed in 3 mL of cyclohexane. 2 mL of the oleylamine SS was added, so the volume was still 5 mL. The particles were placed

in the ultrasonic bath. 15 mL of ethanol was added for a final wash and the particles were centrifuged at 8'000 rpm for 10 minutes. The supernatant was removed, and the particles were redispersed in 2 mL of cyclohexane.

**Synthesis of Cu<sub>3</sub>PdN.** The synthesis for Cu<sub>3</sub>PdN nanocrystals was adapted from the literature. Copper nitrate (0.24 mmol, 60 mg, 1 eq) was dissolved in 7.5 mL of hexadecane in a three-neck flask and stirred. Palladium(II) 2,4- pentadionate (0.08 mmol, 25.2 mg, 0.33 eq) was added and stirred. Distilled oleylamine (7.57 mmol, 2.5 mL, 31 eq) was added and the mixture was degassed for 30 minutes at 50 °C. Under argon, the temperature was increased to 240°C at a rate of 10°C per minute. The mixture was left to react for 15 minutes. The flask was removed from the heating mantle and left to cool to room temperature over the course of an hour. The nanocrystals were purified as described previously. However, contrary to the Cu<sub>3</sub>N nanoparticles, the final centrifugation after the ethanol wash required 10 - 15 minutes at 10,000 rpm to precipitate the nanoparticles.

**Synchrotron X-ray total scattering experiments.** Samples were prepared in 1mm polyamide kapton tube. The samples were measured at beamline P21.1 at DESY in Hamburg, Germany. X-ray total scattering data were collected at room temperature in rapid acquisition mode, using a Perkin Elmer digital X-ray flat panel amorphous silicon detector (2048 × 2048 pixels and 200 × 200 μm pixel size) with a sample-to-detector distance of 380 mm. The incident wavelength of the X-rays was  $\lambda = 0.1220 \text{ \AA}$  (101.62 keV). Calibration of the experimental setup was performed using a Ni standard.

Raw 2D data were corrected for geometrical effects and polarization, then azimuthally integrated to produce 1D scattering intensities versus the magnitude of the momentum transfer  $Q$  (where  $Q = 4\pi \sin \theta/\lambda$  for elastic scattering) using pyFAI and xpdtools.<sup>42, 43</sup> The program xPDFsuite with PDFgetX3 was used to perform the background subtraction, further corrections, and normalization to obtain the reduced total scattering structure function  $F(Q)$ , and Fourier

transformation to obtain the pair distribution function (PDF),  $G(r)$ .<sup>44, 45</sup> For data reduction, the following parameters were used after proper background subtraction:  $Q_{\min} = 0.8 \text{ \AA}^{-1}$ ,  $Q_{\max} = 19 \text{ \AA}^{-1}$ ,  $R_{\text{poly}} = 0.9 \text{ \AA}$ . Modeling and fitting were carried out using Diffpy-CMI or PDFgui.<sup>46, 47</sup>

**XPS and DFT.** X-ray photoelectron spectroscopy (XPS) measurements were performed on a Thermo Scientific K-Alpha spectrometer with a monochromated microfocused Al K $\alpha$  X-ray source ( $h\nu = 1486.7 \text{ eV}$ ) and a spot size of  $400 \text{ }\mu\text{m}$ . The X-ray source was operated at  $6 \text{ mA}$  emission current and  $12 \text{ kV}$  anode bias and a flood gun was used for charge compensation. A pass energy of  $20 \text{ eV}$  was used for all core level and valence spectra. The Thermo Scientific Advantage software package was used for all data analysis. All XPS core level spectra were normalized to the peak height of the main feature in the Cu  $2p_{3/2}$  spectra.

The details of the density functional theory (DFT) calculations for Cu<sub>3</sub>N, including density of states, have been previously reported.<sup>4, 48 49 50</sup> To enable the direct comparison of the theory with the experimental valence spectra, the calculated projected density of states (PDOS) was broadened with a Gaussian to match the experimental broadening of  $600 \text{ meV}$ . The PDOS was weighted by one-electron photoionisation cross sections for the respective orbitals of Cu and N using the Galore software package, based on Scofield cross section values.<sup>51-53</sup>

**NMR measurements.** NMR measurements were recorded at  $298\text{K}$  on Bruker UltraShield 500 MHz spectrometer or a  $600 \text{ MHz}$  Bruker Avance III spectrometer. Regular  $^1\text{H}$  NMR measurement were acquired with a  $30^\circ$  pulse with a recycle delay of  $1.5 \text{ sec}$ . Quantitative  $^1\text{H}$  NMR measurements were acquired with a  $90^\circ$  pulse,  $64\text{k}$  data points,  $20 \text{ ppm}$  spectral width, and a recycle delay of  $30 \text{ sec}$ . DOSY measurements were performed with a double stimulated echo and bipolar gradient pulses (dstebpgp2s). The gradient strength was varied quadratically from 2-95% of the probe's maximum value in 16 or 64 steps. The gradient pulse duration and diffusion delay were optimized to ensure a final attenuation of the signal in the

final increment of less than 10% relative to the first increment. The diffusion coefficients were obtained by fitting a modified Stejskal-Tanner equation to the signal intensity decay:

$$I = I_0 e^{-(\gamma \delta g)^2 D(\Delta - 0.6\delta)}$$

$I$  are the signal intensities,  $D$  are the linear diffusion coefficients,  $\gamma$  is the gyromagnetic ratio of the studied nucleus,  $g$  is the gradient strength,  $\delta$  is the pulsed field gradient duration and  $\Delta$  is the diffusion delay. A correction factor of 0.6 is applied for  $\delta$  due to the smoothed squared pulse shape used for the gradient pulses.<sup>54</sup>

**Other instrumentation.** TEM imaging was done using a JEOL JEM2800 field emission gun microscope operated at 200 kV equipped with a TVIPS XF416ES TEM camera. DLS measurements were conducted on a Malvern Zetasizer Ultra in backscattering mode (173°) in a glass cuvette. All measurements were performed at 25°C after equilibrating inside the system for 240 seconds, sample concentration was tuned to achieve system attenuator values between 9-10. UV-VIS spectra were recorded on a PerkinElmer Lambda 365. FTIR spectra were recorded on a Perkin Elmer Spectrum Two spectrometer (attenuated total reflection, ATR).

## Acknowledgments

We acknowledge DESY (Hamburg, Germany), a member of the Helmholtz Association HGF, for the provision of experimental facilities. Parts of this research were carried out at beamline P21.1, PETRA III. We thank Dr. Soham Banerjee for acquiring the PDF data and helpful advice. A.R. acknowledges the support from the Analytical Chemistry Trust Fund for her CAMS-UK Fellowship. C.K. acknowledges the support from the Department of Chemistry, UCL. The authors acknowledge Dr Stephan Lany from NREL for providing the Cu<sub>3</sub>N DFT calculations.

The authors thank Prof. Raymond Schaak and Dr. Robert William Lord for helpful advice and suggestions regarding the purification procedure.

## **Associated Content**

### **Supporting information**

The Supporting Information is available free of charge at.....

<sup>1</sup>H NMR and X-ray diffractograms, ammonia detection results, TEM images, PDF refinements, FTIR analysis, XPS and PDOS results.

## References

1. Chen, Z.; Sun, C.; Guo, W.; Chen, Z., Colloidal III–V Nitride Quantum Dots. In *Nonmagnetic and Magnetic Quantum Dots*, 2018.
2. Ma, Y.; Xiong, L.; Lu, Y.; Zhu, W.; Zhao, H.; Yang, Y.; Mao, L.; Yang, L., Advanced Inorganic Nitride Nanomaterials for Renewable Energy: A Mini Review of Synthesis Methods. **2021**, 9 (390).
3. Parvzian, M.; De Roo, J., Precursor chemistry of metal nitride nanocrystals. *Nanoscale* **2021**.
4. Zakutayev, A.; Caskey, C. M.; Fioretti, A. N.; Ginley, D. S.; Vidal, J.; Stevanovic, V.; Tea, E.; Lany, S., Defect Tolerant Semiconductors for Solar Energy Conversion. *J Phys Chem Lett* **2014**, 5 (7), 1117-25.
5. Maruyama, T.; Morishita, T., Copper nitride and tin nitride thin films for write-once optical recording media. *Applied Physics Letters* **1996**, 69 (7), 890-891.
6. Yin, Z.; Yu, C.; Zhao, Z.; Guo, X.; Shen, M.; Li, N.; Muzzio, M.; Li, J.; Liu, H.; Lin, H.; Yin, J.; Lu, G.; Su, D.; Sun, S., Cu<sub>3</sub>N Nanocubes for Selective Electrochemical Reduction of CO<sub>2</sub> to Ethylene. *Nano Lett* **2019**, 19 (12), 8658-8663.
7. Panda, C.; Menezes, P. W.; Zheng, M.; Orthmann, S.; Driess, M., In Situ Formation of Nanostructured Core–Shell Cu<sub>3</sub>N–CuO to Promote Alkaline Water Electrolysis. *ACS Energy Letters* **2019**, 4 (3), 747-754.
8. Xi, P.; Xu, Z.; Gao, D.; Chen, F.; Xue, D.; Tao, C.-L.; Chen, Z.-N., Solvothermal synthesis of magnetic copper nitride nanocubes with highly electrocatalytic reduction properties. *RSC Adv.* **2014**, 4 (27), 14206-14209.
9. Bocharov, D.; Anspoks, A.; Timoshenko, J.; Kalinko, A.; Krack, M.; Kuzmin, A., Interpretation of the Cu K-edge EXAFS spectra of Cu<sub>3</sub>N using ab initio molecular dynamics. *Radiation Physics and Chemistry* **2020**, 175.
10. Paniconi, G.; Stoeva, Z.; Doberstein, H.; Smith, R. I.; Gallagher, B. L.; Gregory, D. H., Structural chemistry of Cu<sub>3</sub>N powders obtained by ammonolysis reactions. *Solid State Sciences* **2007**, 9 (10), 907-913.
11. Cui, X. Y.; Soon, A.; Phillips, A. E.; Zheng, R. K.; Liu, Z. W.; Delley, B.; Ringer, S. P.; Stampfl, C., First principles study of 3d transition metal doped Cu<sub>3</sub>N. *Journal of Magnetism and Magnetic Materials* **2012**, 324 (19), 3138-3143.
12. Jacobs, H.; Zachwieja, U., Kupferpalladiumnitride, Cu<sub>3</sub>Pd<sub>x</sub>N mit x = 0,020 und 0,989, Perowskite mit "bindender 3d10-4d10-Wechselwirkung". *Journal of the Less Common Metals* **1991**, 170 (1), 185-190.
13. Hahn, U.; Weber, W., Electronic structure and chemical-bonding mechanism of Cu<sub>3</sub>N, Cu<sub>3</sub>NPd, and related Cu(I) compounds. *Phys Rev B Condens Matter* **1996**, 53 (19), 12684-12693.
14. Gulo, F.; Simon, A.; Kohler, J.; Kremer, R. K., Li-Cu exchange in intercalated Cu<sub>3</sub>N-- with a remark on Cu<sub>4</sub>N. *Angew Chem Int Ed Engl* **2004**, 43 (15), 2032-4.
15. Choi, J.; Gillan, E. G., Solvothermal synthesis of nanocrystalline copper nitride from an energetically unstable copper azide precursor. *Inorg Chem* **2005**, 44 (21), 7385-93.
16. Zachwieja, U.; Jacobs, H., Ammonothermalsynthese von kupfernitrid, Cu<sub>3</sub>N. *Journal of the Less Common Metals* **1990**, 161 (1), 175-184.
17. Juza, R.; Hahn, H., Kupfernitrid Metallamide und Metallnitride. VII. *Zeitschrift für anorganische und allgemeine Chemie* **1939**, 241 (2-3), 172-178.
18. Deshmukh, R.; Zeng, G. B.; Tervoort, E.; Staniuk, M.; Wood, D.; Niederberger, M., Ultrasmall Cu<sub>3</sub>N Nanoparticles: Surfactant-Free Solution-Phase Synthesis, Nitridation Mechanism, and Application for Lithium Storage. *Chemistry of Materials* **2015**, 27 (24), 8282-8288.
19. Egeberg, A.; Warmuth, L.; Riegsinger, S.; Gerthsen, D.; Feldmann, C., Pyridine-based low-temperature synthesis of CoN, Ni<sub>3</sub>N and Cu<sub>3</sub>N nanoparticles. *Chem Commun (Camb)* **2018**, 54 (71), 9957-9960.

20. Wu, H.; Chen, W., Copper nitride nanocubes: size-controlled synthesis and application as cathode catalyst in alkaline fuel cells. *J Am Chem Soc* **2011**, *133* (39), 15236-9.
21. Vaughn li, D. D.; Araujo, J.; Meduri, P.; Callejas, J. F.; Hickner, M. A.; Schaak, R. E., Solution Synthesis of Cu<sub>3</sub>PdN Nanocrystals as Ternary Metal Nitride Electrocatalysts for the Oxygen Reduction Reaction. *Chemistry of Materials* **2014**, *26* (21), 6226-6232.
22. Wang, D.; Li, Y., Controllable synthesis of Cu-based nanocrystals in ODA solvent. *Chem Commun (Camb)* **2011**, *47* (12), 3604-6.
23. Sithole, R. K.; Machogo, L. F. E.; Moloto, M. J.; Gqoba, S. S.; Mubiayi, K. P.; Van Wyk, J.; Moloto, N., One-step synthesis of Cu<sub>3</sub>N, Cu<sub>2</sub>S and Cu<sub>9</sub>S<sub>5</sub> and photocatalytic degradation of methyl orange and methylene blue. *Journal of Photochemistry and Photobiology a-Chemistry* **2020**, 397.
24. Kadzutu-Sithole, R.; Machogo-Phao, L. F. E.; Kolokoto, T.; Zimuwandeyi, M.; Gqoba, S. S.; Mubiayi, K. P.; Moloto, M. J.; Van Wyk, J.; Moloto, N., Elucidating the effect of precursor decomposition time on the structural and optical properties of copper(i) nitride nanocubes. *RSC Advances* **2020**, *10* (56), 34231-34246.
25. De Keukeleere, K.; Coucke, S.; De Canck, E.; Van Der Voort, P.; Delpech, F.; Coppel, Y.; Hens, Z.; Van Driessche, I.; Owen, J. S.; De Roo, J., Stabilization of Colloidal Ti, Zr, and Hf Oxide Nanocrystals by Protonated Tri-n-octylphosphine Oxide (TOPO) and Its Decomposition Products. *Chem Mater* **2017**, *29* (23), 10233-10242.
26. Calcabrini, M.; Van den Eynden, D.; Ribot, S. S.; Pokratath, R.; Llorca, J.; De Roo, J.; Ibáñez, M., Ligand Conversion in Nanocrystal Synthesis: The Oxidation of Alkylamines to Fatty Acids by Nitrate. *JACS Au* **2021**, *1* (11), 1898-1903.
27. Boles, M. A.; Ling, D.; Hyeon, T.; Talapin, D. V., The surface science of nanocrystals. *Nat. Mater.* **2016**, *15* (2), 141-53.
28. Fritzinger, B.; Moreels, I.; Lommens, P.; Koole, R.; Hens, Z.; Martins, J. C., In Situ Observation of Rapid Ligand Exchange in Colloidal Nanocrystal Suspensions Using Transfer NOE Nuclear Magnetic Resonance Spectroscopy. *Journal of the American Chemical Society* **2009**, *131* (8), 3024-3032.
29. Anderson, N. C.; Chen, P. E.; Buckley, A. K.; De Roo, J.; Owen, J. S., Stereoelectronic Effects on the Binding of Neutral Lewis Bases to CdSe Nanocrystals. *J Am Chem Soc* **2018**, *140* (23), 7199-7205.
30. Grote, C.; Chiad, K. J.; Vollmer, D.; Garnweitner, G., Unspecific ligand binding yielding stable colloidal ITO-nanoparticle dispersions. *Chem. Commun.* **2012**, *48* (10), 1464-1466.
31. Dierick, R.; Van den Broeck, F.; De Nolf, K.; Zhao, Q.; Vantomme, A.; Martins, J. C.; Hens, Z., Surface Chemistry of CuInS<sub>2</sub> Colloidal Nanocrystals, Tight Binding of L-Type Ligands. *Chem. Mat.* **2014**, *26* (20), 5950-5957.
32. Oliva-Puigdomènech, A.; De Roo, J.; Kuhs, J.; Detavernier, C.; Martins, J. C.; Hens, Z., Ligand Binding to Copper Nanocrystals: Amines and Carboxylic Acids and the Role of Surface Oxides. *Chem. Mat.* **2019**.
33. Lord, R. W.; Holder, C. F.; Fenton, J. L.; Schaak, R. E., Seeded Growth of Metal Nitrides on Noble-Metal Nanoparticles To Form Complex Nanoscale Heterostructures. *Chemistry of Materials* **2019**, *31* (12), 4605-4613.
34. Dhaene, E.; Billet, J.; Bennett, E.; Van Driessche, I.; De Roo, J., The Trouble with ODE: Polymerization during Nanocrystal Synthesis. *Nano Lett.* **2019**, *19* (10), 7411-7417.
35. Zito, J.; Infante, I., The Future of Ligand Engineering in Colloidal Semiconductor Nanocrystals. *Accounts of Chemical Research* **2021**.
36. Doblas, D.; Kister, T.; Cano-Bonilla, M.; González-García, L.; Kraus, T., Colloidal Solubility and Agglomeration of Apolar Nanoparticles in Different Solvents. *Nano Letters* **2019**, *19* (8), 5246-5252.
37. Castilla-Amoros, L.; Stoian, D.; Pankhurst, J. R.; Varandili, S. B.; Buonsanti, R., Exploring the Chemical Reactivity of Gallium Liquid Metal Nanoparticles in Galvanic Replacement. *J Am Chem Soc* **2020**, *142* (45), 19283-19290.
38. Cui, F.; Yu, Y.; Dou, L.; Sun, J.; Yang, Q.; Schildknecht, C.; Schierle-Arndt, K.; Yang, P., Synthesis of Ultrathin Copper Nanowires Using Tris(trimethylsilyl)silane for High-Performance and Low-Haze Transparent Conductors. *Nano Lett* **2015**, *15* (11), 7610-5.



39. Jeong, S.; Liu, Y.; Zhong, Y.; Zhan, X.; Li, Y.; Wang, Y.; Cha, P. M.; Chen, J.; Ye, X., Heterometallic Seed-Mediated Growth of Monodisperse Colloidal Copper Nanorods with Widely Tunable Plasmonic Resonances. *Nano Lett* **2020**.
40. Chen, Y.; Landes, N. T.; Little, D. J.; Beaulac, R., Conversion Mechanism of Soluble Alkylamide Precursors for the Synthesis of Colloidal Nitride Nanomaterials. *J. Am. Chem. Soc.* **2018**.
41. De Roo, J.; Yazdani, N.; Drijvers, E.; Lauria, A.; Maes, J.; Owen, J. S.; Van Driessche, I.; Niederberger, M.; Wood, V.; Martins, J. C.; Infante, I.; Hens, Z., Probing Solvent–Ligand Interactions in Colloidal Nanocrystals by the NMR Line Broadening. *Chem Mater* **2018**, 30 (15), 5485-5492.
42. Ashiotis, G.; Deschildre, A.; Nawaz, Z.; Wright, J. P.; Karkoulis, D.; Picca, F. E.; Kieffer, J., The fast azimuthal integration Python library:pyFAI. *Journal of Applied Crystallography* **2015**, 48 (2), 510-519.
43. Wright CJ, Z. X., Computer-assisted area detector masking. *Journal of Synchrotron Radiation* **2017**, 24(Pt 2), 506-508.
44. Juhas, P.; Davis, T.; Farrow, C. L.; Billinge, S. J. L., PDFgetX3: a rapid and highly automatable program for processing powder diffraction data into total scattering pair distribution functions. *Journal of Applied Crystallography* **2013**, 46, 560-566.
45. Yang, X.; Juhas, P.; Farrow, C. L.; Billinge, S. J., xPDFsuite: an end-to-end software solution for high throughput pair distribution function transformation, visualization and analysis. *arXiv preprint arXiv:1402.3163* **2014**.
46. P. Juhás, C. L. F., X. Yang, K. R. Knox and S. J. L. Billinge, Complex modeling: a strategy and software program for combining multiple information sources to solve ill posed structure and nanostructure inverse problems. *Acta Crystallographica* **2015**, 562-568.
47. Farrow, C. L.; Juhas, P.; Liu, J. W.; Bryndin, D.; Božin, E. S.; Bloch, J.; Proffen, T.; Billinge, S. J. L., PDFfit2 and PDFgui: computer programs for studying nanostructure in crystals. *Journal of Physics: Condensed Matter* **2007**, 19 (33), 335219.
48. Lany, S., Band-structure calculations for the 3d transition metal oxides in GW. *Physical Review B* **2013**, 87 (8).
49. Stevanović, V.; Lany, S.; Zhang, X.; Zunger, A., Correcting density functional theory for accurate predictions of compound enthalpies of formation: Fitted elemental-phase reference energies. *Physical Review B* **2012**, 85 (11).
50. Lany, S., Semiconducting transition metal oxides. *J Phys Condens Matter* **2015**, 27 (28), 283203.
51. Scofield, J. H., **1973**.
52. J Jackson, A.; M Ganose, A.; Regoutz, A.; G. Egde, R.; O Scanlon, D., Galore: Broadening and weighting for simulation of photoelectron spectroscopy. *Journal of Open Source Software* **2018**, 3 (26).
53. Kalha, C. F., Nathalie; Regoutz, Anna Digitisation of Scofield Photoionisation Cross Section Tabulated Data. figshare. Dataset. . **2020**.
54. Sinnaeve, D., The Stejskal-Tanner equation generalized for any gradient shape-an overview of most pulse sequences measuring free diffusion. *Concepts Magn. Reson. Part A* **2012**, 40A (2), 39-65.

# TOC

